Promoted selectivity of photocatalytic CO_2 reduction to C_2H_4 via hybrid Cu_xCoS_y possessing dual unsaturated sites

Yu Nie [a], Yanfang Li [a], Chao An [a], Xin Tan [a], Zhuofeng Hu [c,*], Jinhua Ye [d], Tao Yu [b,*]

[a] School of Environmental Science and Engineering, Tianjin University, No.135, Yaguan Road, Tianjin 300350, PR China
[b] School of Chemical Engineering and Technology, Tianjin University, No.135, Yaguan Road, Tianjin 300350, PR China
[c] Guangdong Provincial Key Laboratory of Environmental Pollution Control and Remediation Technology, Sun Yat-sen University, No.135, Xingang West Road, Guangzhou 510006, PR China
[d] International Center for Materials Nanoarchitectonics (WPI-MANA) National Institute for Materials Science (NIMS), 1–1 Namiki, Tsukuba 305-0047, Japan

ABSTRACT

Ethylene production by CO_2 reduction is sluggish because the repulsive dipole-dipole interaction and 12 proton-coupled electron-transfer steps consecutively. Amorphous structured photocatalysts possess few grain boundaries and abundant unsaturated sites, accelerating the reaction efficiency from the angle of dynamics and thermodynamics, which still not yet be used in PCR to C_2 products currently. Herein, an amorphous Cu_xCoS_y composed of the minority crystalline $CuCo_2S_4$ is fabricated to realize an excellent C_2H_4 selectivity in terms of $R_{electron}$ (94.9%). Unsaturated Co and S play the key roles in the improved efficiency of C_2H_4 generation. C-C coupling is achieved via shortening Co-S bonds distance, and *CO-*CO coupling barrier is decreased by more electrons accumulated on unsaturated S. Water is adsorbed on Co adjacent to S and provide protons for *COCO to form *$CH_2 = C$. This work paves a new way for broadening the efficient of C_2H_4 photocatalytic evolution using amorphous photocatalyst.

1. Introduction

Photocatalytic conversion of CO_2 with H_2O into solar fuels would be like shooting two hawks with one arrow in terms of saving supplying energy and environment, which occurs mostly on the surfaces of semiconductors through complicated processes involving multi-electrons/protons transfer reactions.[1–3] Deep photoreduction of CO_2 to valued-added or energy-dense products, especially C_{2+} products (C_2H_4, C_2H_6, CH_3CH_2OH and CH_3COOH) is more desirable and challengeable. [4–8] Photocatalysis is considered as a desirable strategy to realize C_2H_4 synthesis through mild and environmentally benign pathways.[9] Most photocatalysts reported so far exhibited poor selectivity less than 67% and low yields lower than 13.4 µmol g^{-1} h^{-1}.[10–18] The reason is that the photogeneration of C_2H_4 from CO_2 is kinetically sluggish because 12 proton-electrons transfer and repulsive dipole-dipole interaction between adjacent carbonaceous. [19].

Recently, amorphous photocatalysts have attracted immense research attentions on account of structural characteristics are completely different from crystals.[20,21] Unsaturated sites can be constructed on amorphous catalysts, fundamentally altering the chemical environment around atoms. These advantages give it the potential for application in photocatalytic CO_2 reduction. The photocatalytic CO_2 reduction on amorphous photocatalyst had been realized, but the photogeneration of C_2H_4 has not yet produced successfully for the reason that C-C cannot coupling.[22–25] Therefore, it is meaningful to modulate electron structure of active sites of amorphous materials to promote PCR to C_2H_4.

Herein, we developed an amorphous Cu_xCoS_y/crystalline $CuCo_2S_4$ composites for PCR, achieved 30.02 µmol g^{-1} h^{-1} C_2H_4 yields with 94.9% selectivity in terms of $R_{electron}$ under visible light irradiation without photosensitizers or sacrificial agents. Few grain boundaries of amorphous Cu_xCoS_y promoted photocurrent densities, offered faster electron transport, and reduced transfer resistance to overcome kinetic limitations. More importantly, the loose structure and long-range disorder allowed ions in the interstitial matrix translational flexibility and altered the electronic structure of dual unsaturated active sites. Amorphous Cu_xCoS_y can theoretically solve the problem of C-C coupling on unsaturated S sites due to Co-S bonds distance shortening, and decrease energy barrier of *CO-*CO coupling as more electrons' existence on unsaturated S sites. Water molecules, adsorbed on Co ions adjacent to S

ions, was split to provide protons for subsequent intermediate $*CH_2=C$ formation. Unsaturated Co and S sites played the promising roles on intermediates generation in the process of PCR to C_2H_4. Crystalline $CuCo_2S_4$(CCS) which performed as cocatalyst facilitated photocarriers separation and Cu in crystalline $CuCo_2S_4$ enhanced CO adsorption to improve C_2H_4 selectivity. Two components collaboratively improved performance in photocatalytic CO_2 to C_2H_4.

2. Experimental

2.1. Materials

Sodium dodecyl sulfate (SDS, Heowns), copper chloride ($CuCl_2$, Kemiou), sodium hydroxide (NaOH, Macklin), hydroxylamine hydro-chloride (Heowns), cobalt chloride (Sinopharm), CH_3OH (Tianjin Jiangtian Chemistry), HCOONa (Heowns), H_2SO_4 (Tianjin Yuanli Chemistry) and C_2H_5OH (Tianjin Yuanli Chemistry) were used. L-cysteine (L-Cys, 98%), and KBr (SP, 99%) were bought from Aladdin. All chemicals were used without further purification.

2.2. Preparation of photocatalyst

10 g SDS and 0.512 g $CuCl_2$ were dissolved in 400 mL DI water, then 30 mL 1 M NaOH was added into above solution. After 15 min stirring, 60 mL 0.2 M hydroxylamine hydrochloride was slowly dropped into above suspension. Stirring for another 30 min and the product was washed with water and alcohol for three times each and dried at 60 ℃ under vacuum. The product was marked as Cu precursor.

0.1 g Cu precursor, 6.6 g $CoCl_2$ and 6.7 g L-Cys were dissolved into 40 mL DI water and then transferred to 100 mL Teflon-lined autoclave with heating at 140 ℃ for 12 h. Finally, the suspension was washed with water and alcohol for three times each, dried at 60 ℃ under vacuum. This sample was amorphous Cu_xCoS_y that denoted as CCS-A.

Usages of $CoCl_2$ and L-Cys were decreased to 2.64 g (1.32 g) and 2.68 g (1.34 g), amorphous/crystalline CuCoS named as CCS-H1 and CCS-H2 were synthesized.

Crystalline $CuCo_2S_4$ that denoted as CCS-C was synthesized as referred to Gopinath and Deka.[26]

2.3. Photocatalytic CO_2 reduction test

Photocatalytic CO_2 reduction was carried out in a sealed system with a 358.8 mL glass reactor in capacity and was strictly vacuumized before reaction. In the process of tests, 20 mg catalyst was ground carefully and dispersed on quartz paper evenly, and 10 mL distilled water was added into reactor. 70 kPa high purity absolute excess CO_2 (99.999%) pumped into system after it was vacuumed, and was kept in dark for adsorption for 30 min. A 300 W Xe lamp with a 420 nm cutoff filter was used as the light source. An GC-2014 was used to detect the content of C_2H_4, CH_4, CO and H_2 each hour. Organics were separated by Sunpak-A (H-2099, 50–80) column, CO went through methanation furnace and separated by Porapak-QS (H-2100, 80–100) column. H_2 was separated by 5 A molecular sieve column. The detectors of organic and CO were FID, and H_2 was detected by TCD. The selectivity of C_2H_4 formation in terms of $R_{electron}$ was calculated by Eq. (1).

$$\% of \quad C_2H_4 \quad selectivy = \frac{12N_{C2H4}}{12N_{C2H4} + 8N_{CH4} + 2N_{CO} + 2N_{H2}} * 100 \quad (1)$$

In this equation, N_{C2H4}, N_{CH4}, N_{CO} and N_{H2} represented the yield of C_2H_4, CH_4, CO and H_2, respectively.

3. Results and discussion

3.1. Structure and morphology

To determine the morphology of photocatalyst, High Resolution

Transmission Electron Microscope (HR-TEM) was used to scan the amorphous hybrid crystalline CCS (CCS-H1) (Figs. 1**a, b,** and **S1**) and amorphous CCS (CCS-A) (Figs. S2–3). Minority crystalline $CuCo_2S_4$ grown on the edge of amorphous Cu_xCoS_y as detected on CCS-H1. The boundary of crystal and amorphous photocatalysts was zoned obviously, and the corresponding Fast Fourier Transform (FFT) obviously reinforced the mixture of crystalline and amorphous structure in CCS-H1 (Fig. 1**b**). CCS-A and CCS-H1 possessed few grain boundaries as HR-TEM displayed. The uniform distribution of Cu, Co and S elements was detected on both amorphous Cu_xCoS_y and crystalline $CuCo_2S_4$ (Figs. 1**b** and **S4,** EDS mapping), and higher Cu element concentrations were on $CuCo_2S_4$ than that of Cu_xCoS_y.

Generally broad peak of X-ray diffraction (XRD) pattern on CCS-A demonstrated its amorphous nature (Fig. 1**c**).[27,28] Peaks at 26.6°, 31.3°, 38.0° and 54.8° on CCS-H1 and CCS-H2 (amorphous CCS hybrid more crystalline CCS) were corresponding to different lattice planes of $CuCo_2S_4$ (JCPDS#42–1450), respectively. It was revealed that CCS-H1 and CCS-H2 were composed by crystalline $CuCo_2S_4$ and amorphous Cu_xCoS_y. Unpaired electrons which were induced by amorphous structure were present in CCS-A, CCS-H1 and CCS-H2 as EPR results displayed (Fig. S5). As we can see, excellent light adsorption capacity of CCS-A, CCS-H1 and CCS-H2 was detected, and the optical adsorption in the whole spectral range of CCS-C had not distinct adsorption edge due to its metallic property (Fig. 1**d**).[29] The conduction band of CCS-A was approximately at − 0.95 V, while valance band was measured by using X-ray photoelectron spectroscopy (XPS) (Fig. S6). Band structures of CCS-A and CCS-C were displayed and proved that CCS-A can accomplish CO_2 reduction from thermodynamics principle (Fig. S6).

To illustrate the chemical state and electron deviation property of as-synthesized photocatalysts, X-ray photoelectron spectroscopy (XPS), synchrotron X-ray absorption near edge structure (XANES) and theoretical calculation were carried out systematically. The wide scan XPS survey spectra of CCS-C, CCS-A and CCS-H1 showed the presence of Cu, Co, S elements (Fig. S7). In high-resolution XPS spectra, two prominent peaks at binding energy of 778.7 and 781.0 eV and second at 793.7 and 797.3 eV corresponding to the Co $2p_{3/2}$ and Co $2p_{1/2}$ spin−orbit peaks (Fig. 2**a**), confirming the existence of two kinds of cobalt oxidation state: Co^{3+} and Co^{2+}.[26,30] Higher energy shift of Co XPS peaks on CCS-A and CCS-H1 in comparison with CCS-C indicated that elevated valence of Co, as the proportion of Co^{3+} changed from 58.2% on CCS-C to 76% on CCS-H1 (Table S1). For S $2p$, two peaks at 161.5 and 162.7 eV were shown, representing S $2p_{3/2}$ and S $2p_{1/2}$ of sulfide (Fig. 2**b**).[31] Two new S $2p$ characteristic peaks in CCS-A and CCS-H1 were attributed to the unsaturated S species.[32] Elements component analysis was further confirmed by Inductively Coupled Plasma-Optical Emission Spectrometer (ICP-OES) and Energy Dispersive Spectroscopy (EDS) mapping (Table S2).

To deep verify the local atomic and electronic structures of CCS-C and CCS-H1, synchrotron XANES was carried out accordingly (Fig. 2**c** and **S8**). A shift to higher energy as compared to the case of CCS-C was observed in CCS-H1, indicating a higher average oxidation state of Co that was matched well with XPS analysis results (Fig. 2**a** and Table S1). Oxidation state of Cu did not change as XANES and XPS results displayed (Fig. S7 and S8), illustrating Cu atom was not the main character of PCR. Co-S bonds distance was 2.41 Å in CCS-C, and was shortened obviously in CCS-A according to theoretical calculation (Fig. 2**d** and Table S3). The shortening of bond distance in CCS-H1 was proved by the subsequent XAS analysis, which just explained why C-C coupling can be achieved at the S sites. It was also obtained directly using theoretical calculation. After structure relaxation, it was found that C-C distance was 1.54 Å which favored the C-C coupling process (Fig. 2**e**). Simultaneously, the distance of C-S was 1.83 Å due to the strong chemical bonds between C and S of CCS-A. And the distance between the two S sites on CCS-A was 2.99 Å while it was 3.34 Å on CCS-C (Fig. S9), which was caused by amorphous structure. Strong chemical bonds between C and S, along with that shortening Co-S can overcome the dipole-dipole interaction on
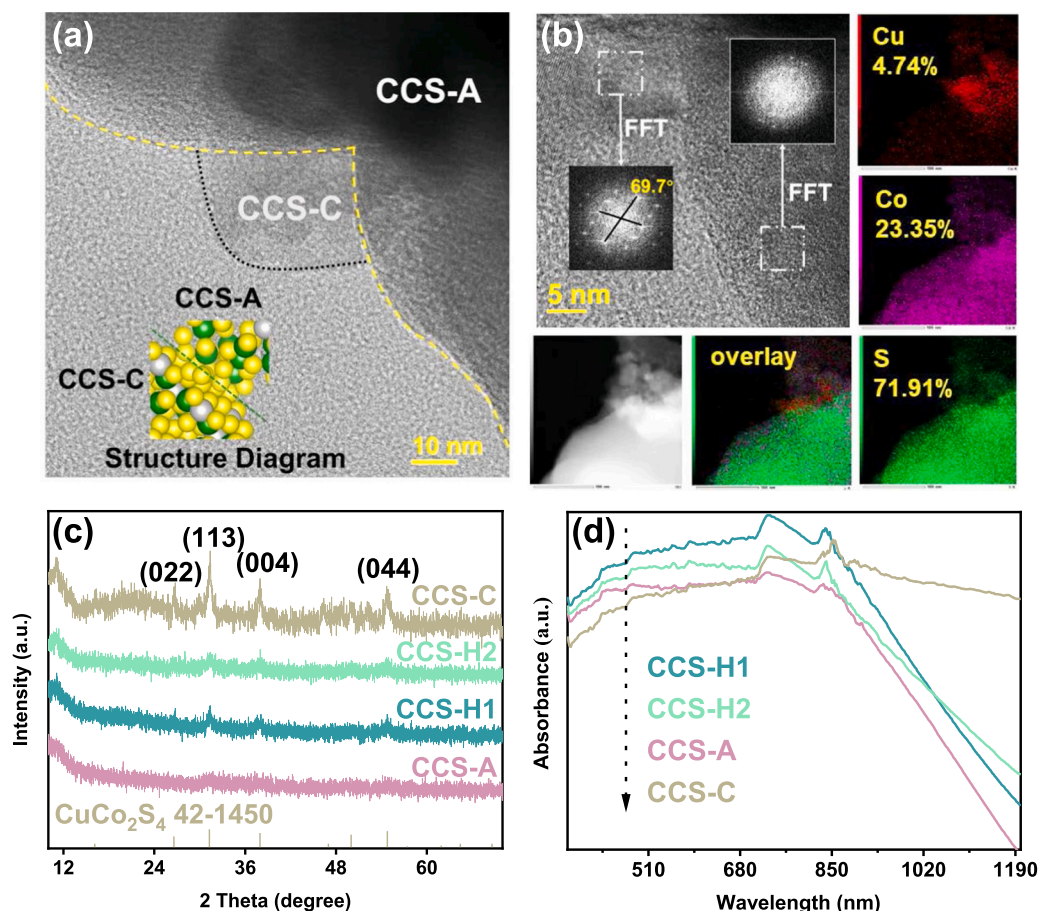
Fig. 1. (a) HR-TEM and structure diagram of CCS-H1. (b) HR-TEM, FFT and EDS mapping of CCS-H1. (c) XRD and (d) DRS of CCS-C, CCS-A, CCS-H1 and CCS-H2.

S sites, were the reason why C-C can couple. Charge distribution was studied by Bader charge analysis (Table S4), confirming S atoms gained electrons as the charge values were larger than that in the isolated state. Logically, the charge of unsaturated S atom near the surface was investigated (Fig. 2f), the unsaturated S atoms exhibited the charge number of 6.33 e, 6.52 e, 6.42 e, 6.45 e and 6.43 e, which were larger than the average values of 6.31 e in CCS-A. XPS analysis and Bader charge distribution suggested that the S atoms near the surface gained more electrons. Logically, the C-C coupling was accomplished because Co-S was shortened, and energy barrier of *CO-*CO coupling was reduced as a result of more electrons accumulated on unsaturated S atoms.

3.2. Photocatalytic CO₂ reduction performance

To demonstrate why the amorphous CCS can boost the photoreduction CO_2 to C_2H_4 under visible light irradiation (λ⟩420 nm) without the addition of photosensitizer or sacrificial agents, the comprehensive PCR experiments were performed on CCS-A, CCS-H1 and CCS-H2 separately. C_2H_4 photogeneration rates were achieved at 0, 20.62, 30.02 and 14.39 $\mu mol\ g^{-1}\ h^{-1}$ on CCS-C, CCS-A, CCS-H1 and CCS-H2 (Fig. 3a). None liquid products that generally methanol and formic acid were produced (Fig. S10). The dominated enhancement was deduced as that CCS-A/H photocatalysts possessed dual unsaturated sites which caused by amorphous structure, and crystalline CCS-C had not, which will be discussed systematically later in this work. As we can see, 94.9% C_2H_4 selectivity in terms of $R_{electron}$ was determined on CCS-H1. The high C_2H_4 selectivity and yields were attributed to faster electrons transfer dynamically, which was induced by few grain boundaries of amorphous structure.[33,34] Consistent with shortening Co-S bonds

distance and more electrons around on S atoms, CCS-A, CCS-H1 and CCS-H2 overcame severe C-C coupling, which proved the superiority of amorphous structure in the process of PCR. It should be noted that CCS-C acted as cocatalyst solely in the process of PCR and no carbon product can be generated (Fig. S11 and Table S5). The C_2H_4 selectivity of CCS-H1 was superhigh as ever reported (Table S6, the summary of reported C_2H_4 selectivity in PCR), and it was first time reported that the amorphous photocatalyst can realize C_2H_4 photogeneration (Table S7, amorphous catalysts for PCR). CCS-A exhibited superb C_2H_4 yields, but its CO yields were also relatively high resulting in low C_2H_4 selectivity. CCS-H1 behaved both yields and high selectivity, the reason for which can be hypothesized to be that CCS-C can enhance CO adsorption. To test the conjecture, we replaced CO_2 with CO as the reaction gas (Fig. 3b and S12). The initial step of reaction is adsorption, so the performance of the CCS-A and CCS-H1 was compared in the first hour. C_2H_4 yields of CCS-H1 were increased after replacing CO as the reaction gas, while it was decreased of CCS-A. This experimental result was consistent with Fig. 3a, and verified our conjecture that the CCS-A was the reactive site to accomplish the reaction from CO_2 to C_2H_4, but its adsorption of CO was slightly weaker so that it had relatively low selectivity. Although CCS-C cannot complete the reaction, they can enhance the CO adsorption, which made CCS-H1 obtained both satisfactory C_2H_4 yields and selectivity. The C_2H_4 yields after three hours of both CCS-A and CCS-H1 was higher when CO was the feed gas than that at CO_2 atmosphere (Fig. S12), because CO is both product and intermediate.

The recombination of electron-holes on the photocatalyst prevents the product from increasing linearly with increasing reaction time. Activity test was also performed in the presence of triethanolamine (TEOA) as a sacrificial agent (Fig. S13). The addition of TEOA resulted in improved performance and linearity. CCS-H1 achieved 95.99 $\mu mol\ g^{-1}$
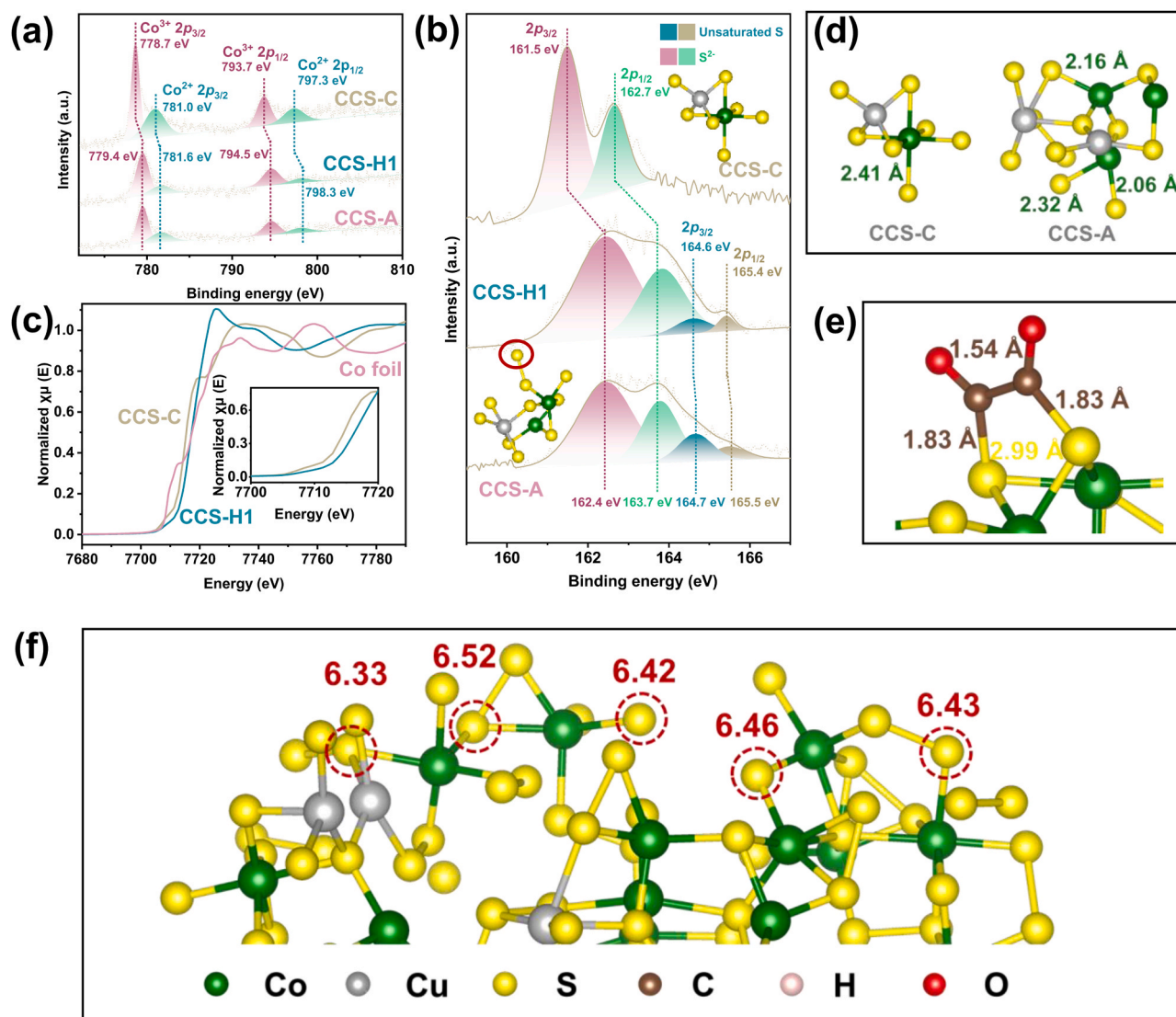
Fig. 2. High resolution XPS of (a) Co *3d* and (b) S *2p* on CCS-C, CCS-A and CCS-H1. (c) Comparison of Co K-edge XANES spectra of CCS-C and CCS-H1. (d) Co-S bond distances of CCS-C and CCS-A. (e) Calculation model of *CO-CO coupling on CCS-A. (f) Charge distribution of unsaturated S atoms near the surface on CCS-A.

at first hour but nonlinear following (Fig. 3**c**). The nonlinear performance after three hours was not only due to the slowing down of electron-holes separation, but also limited by the oxidation half reaction. Selfoxidation was inevitably occurs for sulfide in photocatalytic reaction under pure water without sacrificial agent (Fig. S14). The addition of TEOA greatly inhibited this situation. The C_2H_4 rate was maintained 86.6% at after four successive cycles (Fig. S13). Stability experiments were also tested over different periods of time which proved that CCS-H1 is very stable (Fig. S15). Wave-length-dependent photocatalytic performance on CCS-H1 was measured to evaluate the apparent quantum efficiency (AQY) (Fig. 3**d**), identifying that the driving force was photoexcitation. The corresponding AQY of CCS-H1 at 420, 450, 475, and 500 nm were 1.25%, 1.50%, 1.40% and 1.54%, respectively. To identify the carbon source of photogenerated C_2H_4, the experiment using isotope labeled $^{13}CO_2$ was also conducted, and the products peak sequences of CO, CO_2, and C_2H_4 were shown (Fig. S16), and the ion fragment analysis results of C_2H_4 peak were displayed. The ion fragment peaks for C_2H_4 were all from $^{13}CO_2$, demonstrating that the generated C_2H_4 on CCS-H1 was definitely derived from the reduction of CO_2. The control experiments in the absence of photocatalyst, light irradiation, CO_2 gas or H_2O vapor injection were performed under the same conditions. In dark and in the absence of photocatalyst, no CO and

hydrocarbon products were generated, which demonstrated that the PCR was driven by light on photocatalyst. Trace product in the absence of CO_2 or H_2O proved that the carbon source was from input CO_2 and hydrogen source came from the added H_2O vapor, and trace product existence was attributed to adsorbed CO_2 and H_2O in catalyst.[13,35].

3.3. Mechanisms of photocarriers separation and transfer

To gain better insight into the mechanism of improved photocatalytic CO_2 reduction, the transfer dynamics of photocarriers were comprehensively analyzed. The photocarriers trends were observed by using transient photocurrent and electrochemical impedance spectroscopy spectra (Figs. 4**a** and 4**b**), lower electric resistance in CCS-H1 than CCS-A was reflected by smaller circle radius. Higher photocurrent density of amorphous catalyst than crystalline was induced by amorphous structure lattice disorder.[33,34] No response on transient photocurrent and the lowest resistance on electrochemical impedance spectroscopy spectra of metallic CCS-C proved it acted as a cocatalyst merely. The average photocarriers lifetime was calculated by using the time-resolved photoluminescence (TRPL) spectra (Fig. 4**c**). The average emission lifetime of CCS-H1 (0.55 ns) was shorter than that of CCS-A, identifying the separation efficiency of carriers increased due to the tight interface
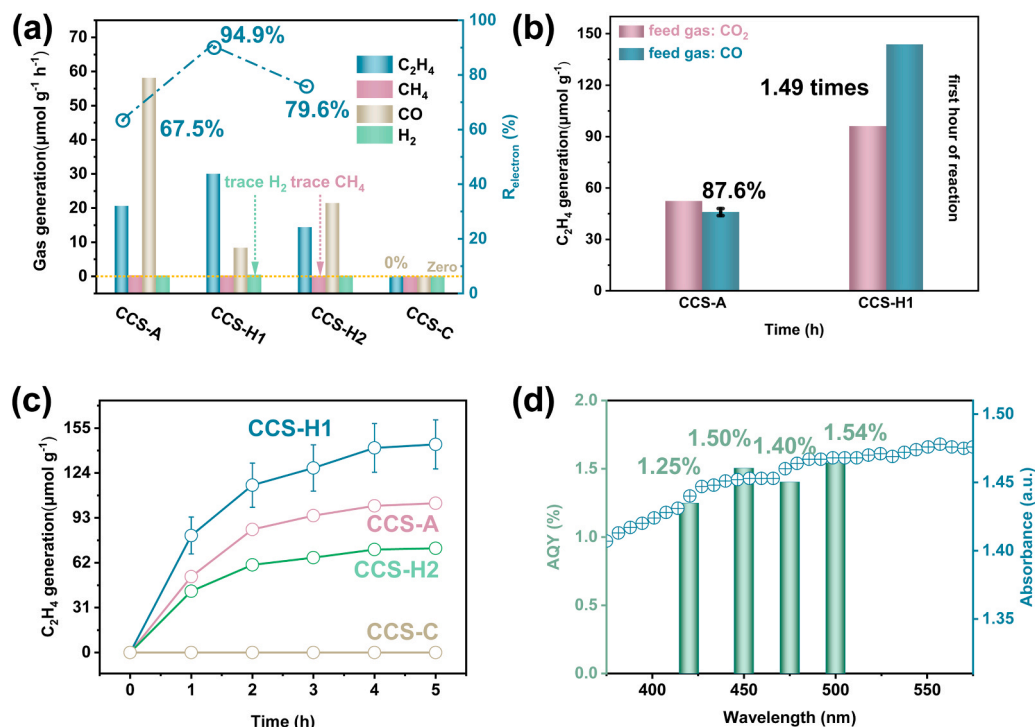
Fig. 3. (a) Photocatalytic CO_2 reduction activities and selectivity in terms of Relectron. (b) Photoreduction CO to C_2H_4 in first hour. (c) Time−yield plots of C_2H_4 on CCS-A, CCS-H1, CCS-H2 and CCS-C. (d) Apparent quantum efficiency (AQY) of CCS-H1.

bonding of CCS-A and CCS-C composites. The lack of adequate electrons supplement induced the desorption of intermediates as the C_1 product, thereafter slowed down the kinetic of 12 electron-transfer process, which hampered the C−C coupling reaction intrinsically. Efficient electrons transfer at the interface of amorphous and crystalline CCS resulted in extended photocarriers lifetime, accelerated migration and separation, thus more electrons were generated to participate in PCR process. The photoluminescence (PL) spectrum of amorphous and hybrid CCS exhibited both peaks at ~400 nm. Compared to peaks of CCS-A at the position on 395 nm, CCS-H1 exhibited peak at 408 nm (Fig. S17). The peaks were corresponding to the relaxation of higher average kinetic energy excited state carriers to lower energy state under 330 nm excitation.[36].

To clarify the separation and transport mechanism of photocarriers at the interface of amorphous and crystalline CCS, CCS-A and CCS-H1 were investigated by using Kelvin-probe force microscopy (KPFM) and surface photovoltage (SPV). More negative SPV signal change before and after light illumination reflected a higher concentration of photogenerated electrons. The CCS-A and CCS-H1 exhibited 8.65 mV and 18.81 mV negative change before and after light illumination (Fig. 4d-i), corresponding to band-to-band transition.[19]. More negative SPV signal change was observed on CCS-H1 than CCS-A exactly demonstrated that cocatalyst minority crystalline $CuCo_2S_4$ enabled to alleviate the electron–holes recombination to achieve high concentration accumulation of photogenerated electrons on the surface. The excess surviving electrons were the prerequisite to photoconversion of CO_2. Obviously, CCS-H1 with minority crystalline $CuCo_2S_4$ achieved higher C_2H_4 photogeneration rates than CCS-A (Fig. 3a). All these pieces of evidence firmly demonstrated that CCS-H1 photocatalyst can enhance the generation, separation, and transport of photoinduced charges, thus rendering high efficiency of PCR.

3.4. Photocatalytic CO_2 pathway and mechanism

The photogenerated electrons were enriched on CCS-H1, the question needed to be illustrated well was whether these photogenerated electrons on the CCS-H1 surface can effectively drive the PCR. To further clarify the PCR mechanism on amorphous surface, relevant in situ experiments, characterizations and theoretical calculations were carried out logically. To provide more detailed information about local cobalt atomic structures, Fourier-transform of the EXAFS $k^3\chi$ data at the Co K-edge was displayed (Fig. 5a). A dominating Co-S peak at 1.82 Å was shown in CCS-C whereas it at 1.74 Å in CCS-H1, which was a powerful supplement to the calculation results (Fig. 2d). *CO-*CO coupling process can be realized when Co-S bonds distance was shortened authentically, resulting the PCR to C_2H_4. The average coordination number of Co atoms of CCS-C was 6 with bond distance of 2.26 Å and 3.6 with distance of 2.22 Å of CCS-H1, which was verified by quantitative EXAFS curve-fitting analyses (Fig. 5b and S18) and was consistent with theoretical calculation results (Fig. 2d).[37] The weaker intensity of the oscillations from CCS-H1 than that of CCS-C was observed, which was attributed to the extent of structure disorder in CCS-H1 as a result of amorphous structure.[38] Few grain boundaries in CCS-H1 reduced the energy consumption of electron migration and accelerated 12 electrons reaction dynamically.[33,34] Wavelet transform (WT) analyses offered a higher resolution in the radial distance more intuitively. The WT intensity maxima near 1.82 and 1.74 Å was associated with Co-S bond in CCS-C and CCS-H1 (Figs. 5c and 5d).

Critically, the mechanism of photocatalytic reduce CO_2 to C_2H_4 still remains ambiguous, especially for the reaction on amorphous photocatalysts, which never be explored clearly up to now (Table. S7). Aimed to this point, the systematically investigations on the photocatalytic mechanism by using in-situ Fourier Transform Infrared spectroscopy (FT-IR) were manipulated. In situ FT-IR was utilized in a continuous steam-saturated carbon dioxide flow (Figs. 5e, 5f and S19). The peaks at 3220 and 3295 cm^{-1} were attributed to the stretching vibrations of C-H on unsaturated $*CH_2 = C$, a vital intermediate for the photogeneration of C_2H_4.[39,40] The peak intensity in CCS-H1 was higher than that of CCS-A which was matched well with experiment results (Fig. 3a). The peaks at 1396, 1450 and 1698 cm^{-1} were assigned to distinct CO_2 adsorption species, and these carbonate species ions can fast diffusion in CCS-A and CCS-H1 in case of their amorphous structure possessed
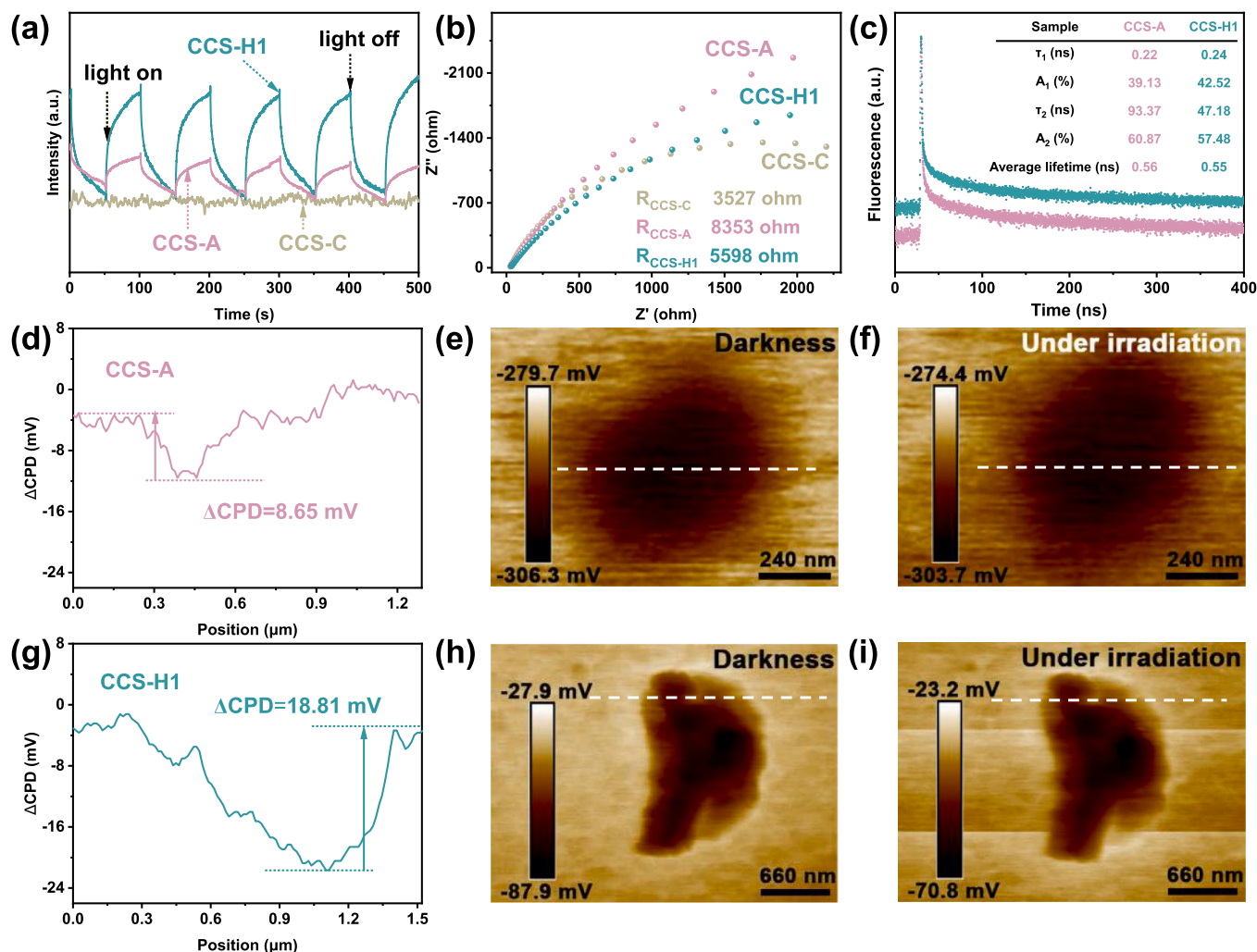
Fig. 4. (a) Transient photocurrent spectra and (b) electrochemical impedance spectroscopy spectra of CCS-A, CCS-H1 and CCS-C. (c) TRPL of CCS-A and CCS-H1. Surface photovoltage change by subtracting the potential under dark conditions from that under illumination ($\Delta CPD = CPD_{dark} - CPD_{light}$) of (d) CCS-A and (g) CCS-H1. SPV images of CCS-A (e) in the dark and (f) under light, and CCS-H1 (h) in the dark and (i) under light.

isotropy.[33] The peak at 1261 cm^{-1} was ascribed to the vibration of *COOH which was first curial intermediate for PCR.[41–43] And the peak at 1650 cm^{-1} was indexed to *COOH or O-H. The peak at 2023 cm^{-1} was chemisorbed CO (*CO) which could couple to form *COCO as result of shortening Co-S bonds distance.[44] The obvious board IR band in the region 1550 cm^{-1} was assigned to the vibrational frequency of the *COCO intermediate according to previous studies.[13, 45] The specie signals of C-C coupling were detected on CCS-A and CCS-H1 because of the existence of the shortening Co-S bonds and unsaturated S sites, which played a key role in improving the coupling efficiency and enriching electrons. Moreover, stronger intensity of IR signals on CCS-H1 than that of on CCS-A were detected validly, affirming the existence of minority crystalline CuCo$_2$S$_4$ was indispensable as CCS-H1 exhibited the highest photocatalytic activity for CO$_2$ reduction. The peak at 1375 cm^{-1} was indexed to *CH$_2$ and the peak at 1445 was assigned to vibration of C=C, reflected that the CCS-A and CCS-H1 were conducive to the product of C$_2$H$_4$ by shortening Co-S bonds distance.[46,47] The *C$_2$H$_4$ intermediate which finally desorbed from the surface was detected at 1689 and 2924 cm^{-1}, indicating the formation of C$_2$H$_4$ instantly in the process of PCR.[44,48].

To intrinsically understand the impact of amorphous on photocatalytic mechanism of C$_2$H$_4$, DFT calculations were actualized accordingly (Figs. 6a and 6b). The Gibbs free energy (ΔG) of the main intermediates during CO$_2$ reduction on CCS-C and CCS-A surfaces were

performed individually. The adsorption free energy for the CO$_2$ molecule was calculated to be −0.23 eV on CCS-C and −0.04 eV on CCS-A, indicating the adsorption of CO$_2$ molecule on their surface was favorable. CO$_2$ molecule was adsorbed on Cu atom in CCS-C, while it was preferred to adsorb on unsaturated Co atom CCS-A. The CO$_2$ adsorption generally facilitates the formation of initial CO$_2$ adducts. The unsaturated Co being a reaction switch and CO$_2$ adsorption site in PCR process. It is well known that the surface adsorption of CO$_2$ is a prerequisite toward the catalytic activity. What's more interesting is that the uptake of CO$_2$ adsorption was promoted obviously, which was ascribed to the unsaturated configuration of Co atoms in CCS-H1 (Fig. S20). Unusual dual unsaturated Co and S atoms were generated in amorphous Cu$_x$CoS$_y$. Unsaturated Co sites can perform as the reaction switch for controlling the proceeding of the reaction.[49].

In PCR process, the transfer of proton and electron to CO$_2$ to generate *COOH intermediate is believed to be the rate-determining step (RDS) on most transition metal-based photocatalysts, due to the high energy barrier required to initiate this process, while reactivity of subsequent C-C coupling reaction will be hampered. *COOH was adsorbed well on CCS-A (−0.04 eV) and C was combined with S sites, showing that *COOH generation was not RDS under amorphous structured condition (Figs. 6a and 6b). However, *COOH was not stably present on CCS-C, leading to the adsorption of C, O and OH in different sites, respectively. The result was that the free energy change was too huge which
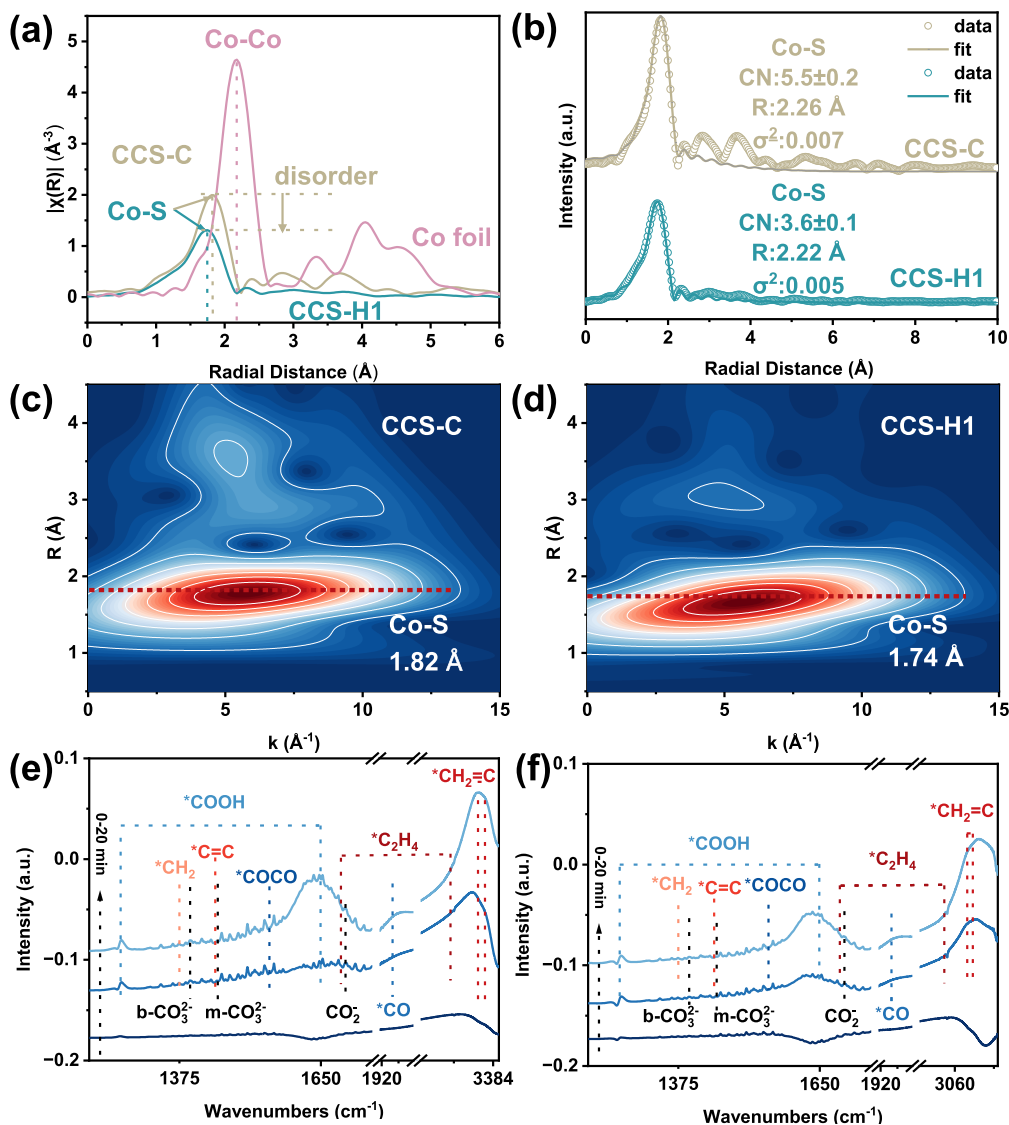
Fig. 5. (a) The comparison of EXAFS, shown in k^2 weighted *R*-space of CCS-C and CCS-H1. (b) Co K-edge EXAFS (points) and fit (line) for the CCS-C and CCS-H1, shown in k^2 weighted R-space. The wavelet transforms of (c) CCS-C and (d) CCS-H1. In-situ FT-IR spectra for co-adsorption of a mixture of CO_2 and H_2O on (e) CCS-H1 and (f) CCS-A.

different from previously reported case. The binding energy of *CO on CCS-A (-0.01 eV) determined the probability of forming higher-carbon products, nevertheless, CO binding energy of CCS-C was -1.79 eV. These results indicated that it was exceedingly easy for CCS-A to form the *COOH intermediate and the *COOH-to-*CO conversion can be readily realized by proton−electron transfer reduction process, the *CO can be coupled because of moderate binding energy soon after. Although CCS-C cannot complete PCR to CO, CCS-C enhanced the adsorption of CO at the edge of CCS-A so reduced product CO selectivity on CCS-H1 (Fig. 3b). While, CO that produced on CCS-A might be desorbed, leading to a not satisfactory enough selectivity (67.5%, Fig. 3a). Meanwhile, in CCS-C, it was precisely Cu atoms that adsorbed CO and CO was adsorbed on Co in CCS-A (Fig. S21). This was the role played by Cu from a thermodynamic perspective.

In this work, the formation of *COCO intermediate was determined as the key step to photogenerated C_2H_4 via energy barrier calculations. *COCO was formed on CCS-A as in-situ FT-IR displayed, and the Gibbs free energies were decreased to -4.67 eV, while it was an endothermic process on CCS-C (0.40 eV). C-C coupling was favored by shorter Co-S bonds distance in CCS-A (less than 2.22 Å) than CCS-C (2.26 Å),

which was proved by XAFS results and theory calculations comprehensively (Figs. 2d and 5a-d). And *CO-*CO coupling energy barrier was decreased on account of that unsaturated S gained more electrons (Fig. 2f). These results strongly indicated that the formation of C_2 products was more favorable on CCS-A. For CCS-C, even CO did not show notable performance toward CO_2 reduction as a result of its crystalline structure without unsaturated atom as active site.

Subsequently, another key step was the formation of $*CH_2 = C$, which was directly detected in our in-situ FT-IR measurement. It was found that the energy dropped on this $*CH_2 = C$ step by proton-electrons coupling. The energy was dropped to -8.69 eV and -10.22 eV for CCS-C and CCS-A, respectively, meaning that the formation of C_2 product would be easy if the *COCO step had been completed. For this process to occur, the protons need to be supplied and were derived from water splitting, consequently, it was important to determine which sites water was adsorbed (Fig. S22). The binding energy of water on Cu and S sites of CCS-C were -0.56 and -0.26 eV, demonstrated water was preferred adsorbed on Cu on CCS-C. For CCS-A, the binding energy of water on Co and S sites were -0.78 and -0.04 eV. The calculation results above proved *CO-*CO coupling occurred on S adjacent to Co and then the
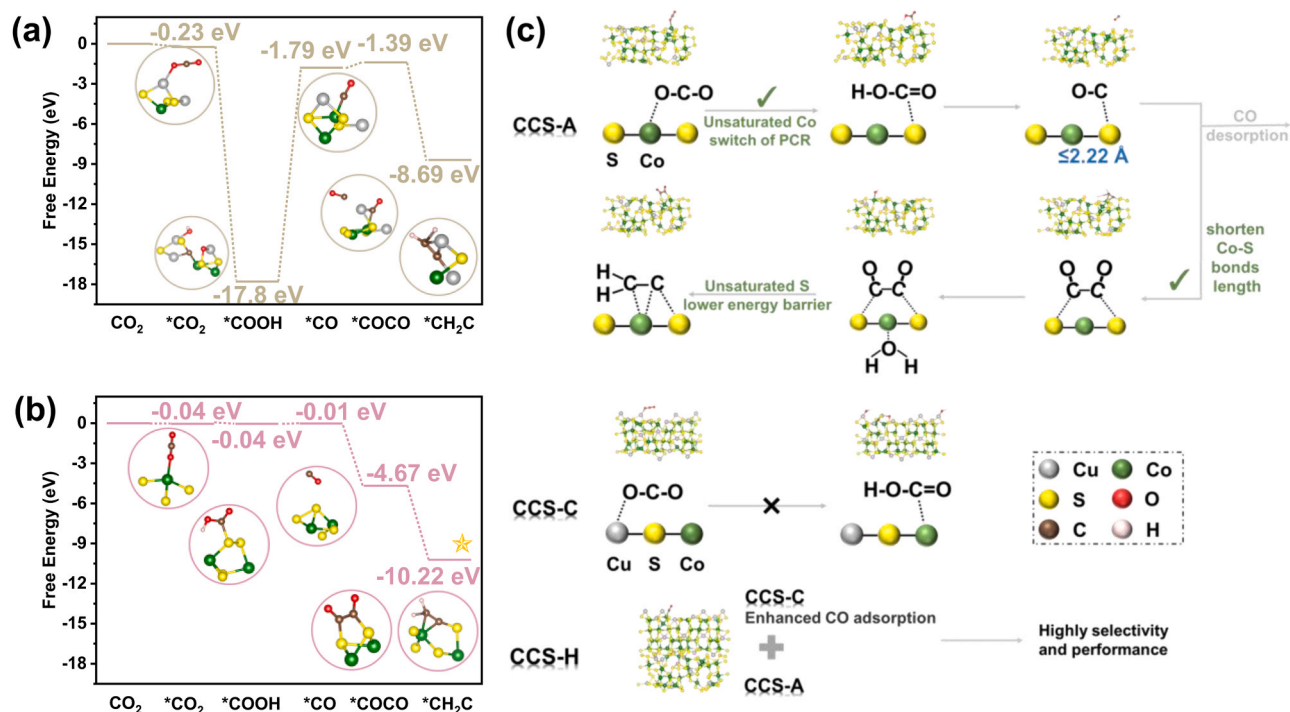
Fig. 6. Gibbs free energy of photocatalytic CO_2 reduction and corresponding chemical molecular structure on (a) CCS-C and (b) CCS-A based on DFT calculations. (c) Schematic diagram of PCR to C_2H_4 on CCS-C, CCS-A and CCS-H.

water adsorbed on Co was dissociated, the generated protons were easier to participate in following proton-electrons transfer to form $*CH_2 = C$ intermediate. The in-situ FT-IR results and DFT calculations manifested significance of amorphous structure for efficient photocatalytic CO_2 to C_2H_4 indeed.

In this context, in-situ FR-IR and DFT calculations were performed to identify crucial intermediates during ethylene formation reaction. XAS and other characterizations were used to analysis the reason why amorphous CCS exhibited such attractive performance. Based on aforementioned results, the reaction paths of PCR to C_2H_4 were summarized as follows (Fig. 6c). In the matter of amorphous/hybrid CCS, unsaturated Co acted as PCR switch so CO_2 can be effectively adsorbed. That CO_2 gone through proton-electron coupling to $*COOH$ was no longer a rate-limiting step which always need huge energy barrier. And the formation of $*CO$ was naturally after CO_2 to $*COOH$. Then formed $*CO$ which adsorbed on S adjacent to Co could occur coupling on account of Co-S bonds distance shortening. Water adsorbed on Co was split to produce protons that simpler joined in subsequent $*CO-*CO$ protonation process to form $*CH_2 = C$. This is the pathway of CCS-A/H for PCR to C_2H_4 and CO desorption was existence on CCS-A. Crystalline CCS was inactive no matter what the beginning of PCR or formation of diverse intermediates. Crystalline CCS lacked unsaturated active sites and cannot reduce the intermediate formation energy so C-C coupling cannot happen. However, CCS-C can increase the adsorption of CO. Consequently, the high C_2H_4 selectivity and production rates of CCS-H1 proved amorphous structure's superiority in CO_2-to-C_2H_4.

4. Conclusions

In summary, amorphous Cu_xCoS_y composed of minority crystalline $CuCo_2S_4$ was synthesized as a photocatalyst for efficient visible-light CO_2 reduction to C_2H_4. Lattice disorder in amorphous Cu_xCoS_y made it accelerate photocurrent and reduced resistance to achieve 12 electrons reaction for C_2H_4 generation. The unsaturated Co atom induced by amorphous structure acted as switch of photocatalytic CO_2 reduction to C_2H_4 and at the same time as CO_2 adsorption sites. CO_2 adsorption was

enhanced on account of unsaturated Co existence, which was demonstrated by adsorption desorption isotherm and DFT calculations. The formation of $*COOH$ was a process that no longer required super energy for amorphous Cu_xCoS_y. C-C coupling became possible as a result of Co-S bonds distance shortening and C-C coupling energy barrier was reduced owing to unsaturated S atom in amorphous catalyst gained more electrons. The water adsorbed on Co was dissociated and the generated protons were easier to participate in proton-electrons transfer to form $*CH_2 = C$ intermediate because $*CO-*CO$ adsorbed on S adjacent to Co. It was demonstrated that crystalline $CuCo_2S_4$ performed as cocatalyst, improving photocatalyst's photoelectrons-holes separation and transfer further. Meanwhile, CO adsorption was enhanced at Cu atoms on crystalline $CuCo_2S_4$. As a result, CCS-H1 achieved 30.02 μmol g^{-1} h^{-1} C_2H_4 evolution rates with 94.9% selectivity in terms of $R_{electron}$. This is the first time that amorphous catalyst used for photocatalytic CO_2 reduction to C_2H_4 and its our pleasure to propose novel understandings and mechanisms.

Supporting information

Experimental sections, characterizations instruments, details of test, computational details and results, XPS, ICP-OES, HR-TEM, EPR, Mott-Schottky, UPS, SPV, XANES, XRD, photoluminescence, EXAFS, CO_2 adsorption and desorption, and N_2 adsorption and desorption had been provided in Supporting information.

Author Contributions

Tao Yu established the research line and supervised the current work; Xin Tan co-supervised the current work; Yu Nie performed the experiments, data analysis and wrote the manuscript. Yanfang Li, Chao An drafted figures and performed the experiments. Zhuofeng Hu provided theoretical calculations. Jinhua Ye provided resources. All the authors reviewed, approved, and contributed to the final version of the manuscript.

Funding

This work was supported by National Key R&D Program of China (2021YFA1500700), the National Natural Science Foundation of China (22066022) (51902357), Ministry of Education, P. R. China, the Fundamental Research Funds for the Central Universities, Sun Yat-sen University (22lgqb23), the Guangzhou Basic and Applied Basic Research Foundation, China (202201011695).

CRediT authorship contribution statement

Yu Nie: Data curation, Writing – original draft, Writing – review & editing. **Tao Yu:** Funding acquisition, Project administration, Resources, Supervision, Writing – review & editing. **Jinhua Ye:** Resources. **Chao An:** Visualization, Writing – review & editing. **Yanfang Li:** Visualization, Writing – review & editing. **Zhuofeng Hu:** Resources, Software, Writing – review & editing, Funding acquisition. **Xin Tan:** Resources.

Declaration of Competing Interest

We declare that we have no financial and personal relationships with other people or organizations that can inappropriately influence our work, there is no professional or other personal interest of any nature or kind in any product, service and/or company that could be construed as influencing the position presented in, or the review of, the manuscript entitled.

Data availability

Data will be made available on request.

Acknowledgement

Appendix A. Supporting information

Supplementary data associated with this article can be found in the online version at doi:10.1016/j.apcatb.2024.123704.

References

[1] W. Tu, Y. Zhou, Z. Zou, Photocatalytic conversion of CO_2 into renewable hydrocarbon fuels: state-of-the-art accomplishment, challenges, and prospects, Adv. Mater. 26 (2014) 4607–4626.

[2] G. Wang, J. Chen, Y. Ding, P. Cai, L. Yi, Y. Li, C. Tu, Y. Hou, Z. Wen, L. Dai, Electrocatalysis for CO2 conversion: from fundamentals to value-added products, Chem. Soc. Rev. 50 (2021) 4993–5061.

[3] B.M. Tackett, E. Gomez, J.G. Chen, Net reduction of CO2 via its thermocatalytic and electrocatalytic transformation reactions in standard and hybrid processes, Nat. Catal. 2 (2019) 381–386.

[4] A. Dokania, A. Ramirez, A. Bavykina, J. Gascon, Heterogeneous catalysis for the valorization of CO2: role of bifunctional processes in the production of chemicals, ACS Energy Lett. 4 (2018) 167–176.

[5] D.L. Meng, M.D. Zhang, D.H. Si, M.J. Mao, Y. Hou, Y.B. Huang, R. Cao, Highly selective tandem electroreduction of CO2 to ethylene over atomically isolated nickel-nitrogen site/copper nanoparticle catalysts, Angew. Chem. 60 (2021) 25485–25492.

[6] W. Tu, Y. Zhou, Q. Liu, S. Yan, S. Bao, X. Wang, M. Xiao, Z. Zou, An in situ simultaneous reduction-hydrolysis technique for fabrication of TiO2-graphene 2D sandwich-like hybrid nanosheets: graphene-promoted selectivity of photocatalytic-driven hydrogenation and coupling of CO2 into methane and ethane, Adv. Funct. Mater. 23 (2013) 1743–1749.

[7] D. Gao, R.M. Arán-Ais, H.S. Jeon, B. Roldan Cuenya, Rational catalyst and electrolyte design for CO2 electroreduction towards multicarbon products, Nat. Catal. 2 (2019) 198–210.

[8] Q. Lu, F. Jiao, Electrochemical CO2 reduction: electrocatalyst, reaction mechanism, and process engineering, Nano Energy 29 (2016) 439–456.

[9] W. Jiang, J. Low, K. Mao, D. Duan, S. Chen, W. Liu, C.W. Pao, J. Ma, S. Sang, C. Shu, X. Zhan, Z. Qi, H. Zhang, Z. Liu, X. Wu, R. Long, L. Song, Y. Xiong, Pd-modified ZnO-Au enabling alkoxy intermediates formation and dehydrogenation for photocatalytic conversion of methane to ethylene, JACS 143 (2021) 269–278.

[10] X. Luo, L. Qiao, S. Zhang, Q. Li, Y. Liao, S. Rao, H. Liu, Y. Zhao, S-vacancy-assisted dual-sites on NiCo2S4 for photoconversion of CO2 to olefiant gas, Appl. Surf. Sci. 601 (2022) 154184.

[11] W. Shao, X. Li, J. Zhu, X. Zu, L. Liang, J. Hu, Y. Pan, J. Zhu, W. Yan, Y. Sun, Y. Xie, Metal^{n+}-metal$^{δ+}$ pair sites steer C-C coupling for selective CO2 photoreduction to C2 hydrocarbons, Nano. Res. 15 (2021) 1882–1891.

[12] W. Wang, C. Deng, S. Xie, Y. Li, W. Zhang, H. Sheng, C. Chen, J. Zhao, Photocatalytic C-C coupling from carbon dioxide reduction on copper oxide with mixed-valence copper(I)/copper(II), JACS 143 (2021) 2984–2993.

[13] T. Wang, L. Chen, C. Chen, M. Huang, Y. Huang, S. Liu, B. Li, Engineering catalytic interfaces in Cu$^{δ+}$/CeO2-TiO2 photocatalysts for synergistically boosting CO2 reduction to ethylene, ACS Nano 16 (2022) 2306–2318.

[14] C. Chen, T. Wang, K. Yan, S. Liu, Y. Zhao, B. Li, Photocatalytic CO2 reduction on cu single atoms incorporated in ordered macroporous TiO2 toward tunable products, Inorg. Chem. Front. 9 (2022) 4753–4767.

[15] J. Park, H. Liu, G. Piao, U. Kang, H.W. Jeong, C. Jánáky, H. Park, Synergistic conversion of CO2 into C1 and C2 gases using hybrid in-doped TiO2 and g-C3N4 photocatalysts, Chem. Eng. J. 437 (2022) 135388.

[16] Q. Chen, X. Chen, M. Fang, J. Chen, Y. Li, Z. Xie, Q. Kuang, L. Zheng, Photo-induced Au–Pd alloying at TiO2 {101} facets enables robust CO2 photocatalytic reduction into hydrocarbon fuels, J. Mater. Chem. A 7 (2019) 1334–1340.

[17] W. Gao, X. Bai, Y. Gao, J. Liu, H. He, Y. Yang, Q. Han, X. Wang, X. Wu, J. Wang, F. Fan, Y. Zhou, C. Li, Z. Zou, Anchoring of black phosphorus quantum dots onto WO3 nanowires to boost photocatalytic CO2 conversion into solar fuels, Chem. Commun. 56 (2020) 7777–7780.

[18] T. Phongamwong, M. Chareonpanich, J. Limtrakul, Role of chlorophyll in spirulina on photocatalytic activity of CO2 reduction under visible light over modified N-doped TiO2 photocatalysts, Appl. Catal. B Environ. 168-169 (2015) 114–124.

[19] W. Gao, S. Li, H. He, X. Li, Z. Cheng, Y. Yang, J. Wang, Q. Shen, X. Wang, Y. Xiong, Y. Zhou, Z. Zou, Vacancy-defect modulated pathway of photoreduction of CO2 on single atomically thin AgInP2S6 sheets into olefiant gas, Nat. Commun. 12 (2021) 4747.

[20] C.T. Toh, H. Zhang, J. Lin, A.S. Mayorov, Y.P. Wang, C.M. Orofeo, D.B. Ferry, H. Andersen, N. Kakenov, Z. Guo, I.H. Abidi, H. Sims, K. Suenaga, S.T. Pantelides, B. Ozyilmaz, Synthesis and properties of free-standing monolayer amorphous carbon, Nature 577 (2020) 199–203.

[21] S. Chen, A. Tennakoon, K.-E. You, A.L. Paterson, R. Yappert, S. Alayoglu, L. Fang, X. Wu, T.Y. Zhao, M.P. Lapak, M. Saravanan, R.A. Hackler, Y.-Y. Wang, L. Qi, M. Delferro, T. Li, B. Lee, B. Peters, K.R. Poeppelmeier, S.C. Ammal, C.R. Bowers, F. A. Perras, A. Heyden, A.D. Sadow, W. Huang, Ultrasmall amorphous zirconia nanoparticles catalyse polyolefin hydrogenolysis, Nat. Catal. 6 (2023) 161–173.

[22] Y. Li, B. Li, D. Zhang, L. Cheng, Q. Xiang, Crystalline carbon nitride supported copper single atoms for photocatalytic CO2 reduction with nearly 100% CO selectivity, ACS Nano 14 (2020) 10552–10561.

[23] G. Yin, X. Huang, T. Chen, W. Zhao, Q. Bi, J. Xu, Y. Han, F. Huang, Hydrogenated blue titania for efficient solar to chemical conversions: preparation, characterization, and reaction mechanism of CO2 reduction, ACS Catal. 8 (2018) 1009–1017.

[24] H. Yang, D. Yang, X. Wang, POM-incorporated CoO nanowires for enhanced photocatalytic syngas production from CO2, Angew. Chem. 59 (2020) 15527–15531.

[25] F. Fresno, P. Reñones, E. Alfonso, C. Guillén, J.F. Trigo, J. Herrero, L. Collado, V. A. de la Peña O'Shea, Influence of surface density on the CO2 photoreduction activity of a DC magnetron sputtered TiO2 catalyst, Appl. Catal. B Environ. 224 (2018) 912–918.

[26] M. Chauhan, K.P. Reddy, C.S. Gopinath, S. Deka, Copper cobalt sulfide nanosheets realizing a promising electrocatalytic oxygen evolution reaction, ACS Catal. 7 (2017) 5871–5879.

[27] J.S. Kim, I. Park, E.S. Jeong, K. Jin, W.M. Seong, G. Yoon, H. Kim, B. Kim, K. T. Nam, K. Kang, Amorphous cobalt phyllosilicate with layered crystalline motifs as water oxidation catalyst, Adv. Mater. 29 (2017).

[28] K.K. Kumar, M. Ravi, Y. Pavani, S. Bhavani, A.K. Sharma, V.V.R. Narasimha Rao, Investigations on PEO/PVP/NaBr complexed polymer blend electrolytes for electrochemical cell applications, J. Membr. Sci. 454 (2014) 200–211.

[29] Y. Guo, L. Mao, Y. Tang, Q. Shang, X. Cai, J. Zhang, H. Hu, X. Tan, L. Liu, H. Wang, T. Yu, J. Ye, Concentrating electron and activating H-OH bond of absorbed water on metallic NiCo2S4 boosting photocatalytic hydrogen evolution, Nano Energy 95 (2022) 107028.

[30] H. Zhu, J. Zhang, R. Yanzhang, M. Du, Q. Wang, G. Gao, J. Wu, G. Wu, M. Zhang, B. Liu, J. Yao, X. Zhang, When cubic cobalt sulfide meets layered molybdenum disulfide: a core-shell system toward synergetic electrocatalytic water splitting, Adv. Mater. 27 (2015) 4752–4759.

[31] Y. Zhang, W. Zhou, Y. Tang, Y. Guo, Z. Geng, L. Liu, X. Tan, H. Wang, T. Yu, J. Ye, Unravelling unsaturated edge S in amorphous NiSx for boosting photocatalytic H2 evolution of metastable phase CdS confined inside hydrophilic beads, Appl. Catal. B Environ. 305 (2022) 121055.

[32] Q. Xu, Y. Liu, H. Jiang, Y. Hu, H. Liu, C. Li, Unsaturated sulfur edge engineering of strongly coupled MoS2 nanosheet-carbon macroporous hybrid catalyst for enhanced hydrogen generation, Adv. Energy, Mater. 9 (2019) 1802553.

[33] D. Yang, R. Yang, J. Zhang, Z. Yang, S. Liu, C. Li, High efficiency flexible perovskite solar cells using superior low temperature TiO2, Energ. Environ. Sci. 8 (2015) 3208–3214.

[34] B. Wang, M. Zhang, X. Cui, Z. Wang, M. Rager, Y. Yang, Z. Zou, Z.L. Wang, Z. Lin, Unconventional route to oxygen-vacancy-enabled highly efficient electron extraction and transport in perovskite solar cells, Angew. Chem. 59 (2020) 1611–1618.

[35] Y. Li, Z. Ren, M. Gu, Y. Duan, W. Zhang, K. Lv, Synergistic effect of interstitial C doping and oxygen vacancies on the photoreactivity of TiO_2 nanofibers towards CO_2 reduction, Appl. Catal. B Environ. 317 (2022) 121773.

[36] B.L. Liao, E. Najafi, H. Li, A.J. Minnich, A.H. Zewail, Photo-excited hot carrier dynamics in hydrogenated amorphous silicon imaged by 4D electron microscopy, Nat. Nanotechnol. 12 (2017) 871.

[37] Y. Zhang, B. Xia, J. Ran, K. Davey, S.Z. Qiao, Atomic-level reactive sites for semiconductor-based photocatalytic CO_2 reduction, Adv. Energy, Mater. 10 (2020) 1903879.

[38] Z. Xiao, Y. Wang, Y.-C. Huang, Z. Wei, C.-L. Dong, J. Ma, S. Shen, Y. Li, S. Wang, Filling the oxygen vacancies in Co_3O_4 with phosphorus: an ultra-efficient electrocatalyst for overall water splitting, Energ. Environ. Sci. 10 (2017) 2563–2569.

[39] L. Wang, B. Zhao, C. Wang, M. Sun, Y. Yu, B. Zhang, Thermally assisted photocatalytic conversion of CO_2–H_2O to C_2H_4 over carbon doped In_2S_3 nanosheets, J. Mater. Chem. A 8 (2020) 10175–10179.

[40] C.Wang Chia, Philipp Zielke, Oʹmar F. Sigurbjornsson, C.R. Viteri, R. Signorell, Infrared spectra of C_2H_6, C_2H_4, C_2H_2, and CO_2 aerosols potentially formed in Titan's atmosphere, J. Phys. Chem. A 113 (2009) 11129–11137.

[41] M. Wang, M. Shen, X. Jin, J. Tian, M. Li, Y. Zhou, L. Zhang, Y. Li, J. Shi, Oxygen vacancy generation and stabilization in CeO^{2-x} by Cu introduction with improved CO_2 photocatalytic reduction activity, ACS Catal. 9 (2019) 4573–4581.

[42] J. Sheng, Y. He, J. Li, C. Yuan, H. Huang, S. Wang, Y. Sun, Z. Wang, F. Dong, Identification of halogen-associated active sites on bismuth-based perovskite quantum dots for efficient and selective CO_2-to-CO photoreduction, ACS Nano 14 (2020) 13103–13114.

[43] X.F. Qiu, H.L. Zhu, J.R. Huang, P.Q. Liao, X.M. Chen, Highly selective CO_2 electroreduction to C_2H_4 using a metal-organic framework with dual active sites, JACS 143 (2021) 7242–7246.

[44] R. Xu, D.-H. Si, S.-S. Zhao, Q.-J. Wu, X.-S. Wang, T.-F. Liu, H. Zhao, R. Cao, Y.-B. Huang, Tandem photocatalysis of CO_2 to C_2H_4 via a synergistic rhenium-(I) bipyridine/copper-porphyrinic triazine framework, J. Am. Chem. Soc. (2023).

[45] Y. Kim, S. Park, S.-J. Shin, W. Choi, B.K. Min, H. Kim, W. Kim, Y.J. Hwang, Time-resolved observation of C–C coupling intermediates on Cu electrodes for selective electrochemical CO_2 reduction, Energ. Environ. Sci. 13 (2020) 4301–4311.

[46] F. Guo, R.X. Li, S. Yang, X.Y. Zhang, H. Yu, J.J. Urban, W.Y. Sun, Designing heteroatom-codoped iron metal-organic framework for promotional photoreduction of carbon dioxide to ethylene, Angew. Chem. 62 (2023) e202216232.

[47] R. Zhang, H. Wang, S. Tang, C. Liu, F. Dong, H. Yue, B. Liang, Photocatalytic oxidative dehydrogenation of ethane using CO_2 as a soft oxidant over Pd/TiO_2 catalysts to C_2H_4 and syngas, ACS Catal. 8 (2018) 9280–9286.

[48] Y. Yu, X. Dong, P. Chen, Q. Geng, H. Wang, J. Li, Y. Zhou, F. Dong, Synergistic effect of Cu single atoms and Au-Cu alloy nanoparticles on TiO_2 for efficient CO_2 photoreduction, ACS Nano 15 (2021) 14453–14464.

[49] H. Zhang, Y. Wang, S. Zuo, W. Zhou, J. Zhang, X.W.D. Lou, Isolated cobalt centers on $W_{18}O_{49}$ nanowires perform as a reaction switch for efficient CO_2 photoreduction, JACS 143 (2021) 2173–2177.